Article

Origin of High Activity and Durability of Twisty Nanowire Alloy Catalysts under Oxygen Reduction and Fuel Cell Operating Conditions

Zhijie Kong, Yazan Maswadeh, Jorge A. Vargas, Shiyao Shan, Zhi-Peng Wu, Haval Kareem, Asher C. Leff, Dat T. Tran, Fangfang Chang, Shan Yan, Sanghyun Nam, Xingfang Zhao, Jason M. Lee, Jin Luo, Sarvjit Shastri, Gang Yu,* Valeri Petkov,* and Chuan-Jian Zhong*

Read Online

ACCESS | Metrics & More | Article Recommendations | Supporting Information

ABSTRACT: The ability to control the surface composition and morphology of alloy catalysts is critical for achieving high activity and durability of catalysts for oxygen reduction reaction (ORR) and fuel cells. This report describes an efficient surfactant-free synthesis route for producing a twisty nanowire (TNW) shaped platinum−iron (PtFe) alloy catalyst (denoted as PtFe TNWs) with controllable bimetallic compositions. PtFe TNWs with an optimal initial composition of ~24% Pt are shown to exhibit the highest mass activity (3.4 A/mg$_{Pt}$, ~20 times higher than that of commercial Pt catalyst) and the highest durability (<2% loss of activity after 40 000 cycles and <30% loss after 120 000 cycles) among all PtFe-based nanocatalysts under ORR or fuel cell operating conditions reported so far.

Using ex situ and in situ synchrotron X-ray diffraction coupled with atomic pair distribution function (PDF) analysis and 3D modeling, the PtFe TNWs are shown to exhibit mixed face-centered cubic (fcc)−body-centered cubic (bcc) alloy structure and a significant lattice strain. A striking finding is that the activity strongly depends on the composition of the as-synthesized catalysts and this dependence remains unchanged despite the evolution of the composition of the different catalysts and their lattice constants under ORR or fuel cell operating conditions. Notably, dealloying under fuel cell operating condition starts at phase-segregated domain sites leading to a final fcc alloy structure with subtle differences in surface morphology. Due to a subsequent realloying and the morphology of TNWs, the surface lattice strain observed with the as-synthesized catalysts is largely preserved. This strain and the particular facets exhibited by the TNWs are believed to be responsible for the observed activity and durability enhancements. These findings provide new insights into the correlation between the structure, activity, and durability of nanoalloy catalysts and are expected to energize the ongoing effort to develop highly active and durable low-Pt-content nanowire catalysts by controlling their alloy structure and morphology.
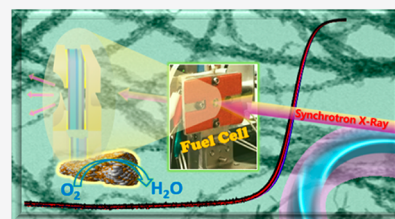
1. INTRODUCTION

The high efficiency and environmental sustainability of proton-exchange-membrane fuel cells (PEMFCs) have attracted increasing interests in the global sustainable energy drive. However, the prohibitive cost and unsatisfactory activity/durability of the Pt/C catalyst have been the greatest obstacle to the commercialization of PEMFCs. Efforts have been devoted to the development of Pt-based catalysts for oxygen reduction reaction (ORR).[1−6] Most reports about composition and activity or durability relationship are based on standard half-cell measurements of Pt-based nanoparticle (NP) catalysts, but testing them in membrane electrode assemblies (MEA) showed poor performance. Pt-based nanowires have shown to enhance activity and long-term stability.[7−9] The understanding of factors (e.g., surface strain, ligand effect, composition, facet, shape, etc.) influencing the activity and stability requires studies under MEA and fuel cell conditions.[10] It has been claimed that Pt$_3$M (M = Ni, Fe, and Co) is the best composition for ORR.[11−13] However, there are some examples

of well-ordered alloy PtFe and core@shell Fe@Pt nanoparticles showing better performance at 50% Fe.[14−16] Theoretically Pt-skinned PtFe$_3$ (111) is suggested to be better than Pt-skinned Pt$_3$Fe(111).[17] For PtCo NP catalysts, the final elemental distribution of PtCo NPs under operating conditions was reported to be directly related to the initial atomic ratio of fresh NPs based on in situ X-ray absorption spectroscopy.[18] The effect of Co content on structure and activity[19] was found to tune (111) facets, showing a maximum at Pt$_{73}$Co$_{27}$ in the Pt-skin/PtCo(111),[19] ORR activity of 27 times larger than that for Pt(111), and overall activity in the order (100) < (110) ≪ (111) facets. In another study of the Pt$_3$Ni (111) crystal facets,[12] the presence of the (111) facet, especially for Pt$_3$Ni
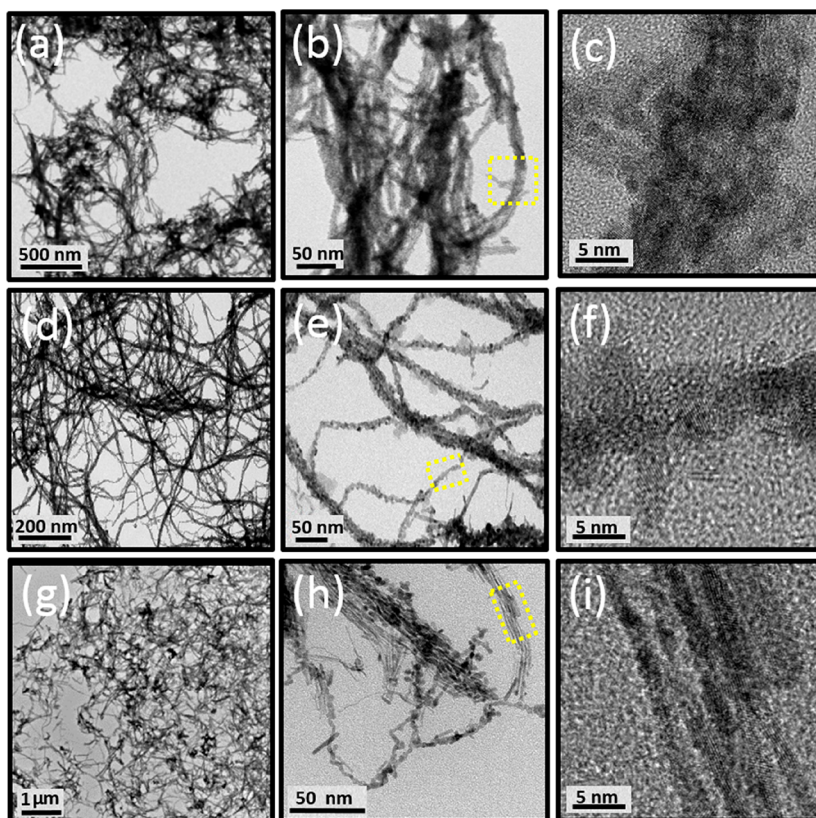
Figure 1. Transmission electron microscopy (TEM) images of representative samples of as-synthesized $Pt_{24}Fe_{76}$ (a−c), $Pt_{42}Fe_{58}$ (d−f), and $Pt_{71}Fe_{29}$ (g−i) nanowires at different magnifications. Images (c, f, g) are magnified views of the yellow-boxed areas of images (b, e, h), respectively. See SEM images in Figure S2 for the general morphology of samples of these NWs.

(111), was found to enhance activity by a factor of 10 for ORR than the corresponding Pt (111). Dealloying of Pt-alloy NPs is shown to exhibit high activity and high durability by controlling the porous morphology.[20,21] Dealloying of $PtNi_3$ NPs showed high activity and durability by controlling nanopore formation to improve the stability.[20] The specific activity is shown to drop drastically along the steep Pt−O strong binding leg upon dealloying.[22] The mass activity is shown to increase after 30 000 cycles of operation in PEMFCs, during which Ni dissolution has a beneficial impact on the Pt−O weak binding to maintain the high activity and minimize site-blocking effect. A small (4%) change in composition was observed after 5000 potential cycles.[23] High activity (0.7 A/mg_{Pt}) and durability (20 000 cycles) were also reported for ORR on ordered face-centered tetragonal (fct) FePt catalysts synthesized by thermal annealing.[24,25]

Despite the significant progress, little has been reported for the composition effect on the activity and durability of PtFe nanowires (NWs). Enhanced ORR activities are attributed to high-density (111) facets on Pt alloy NWs.[26,27] PtNi NWs were found to be stable under ORR condition, showing 11% activity decay after 30 000 cycles.[26] In a previous report on the stability of high-Pt PtFe nanowires,[28] acid washed $Pt_{44}Fe_{56}$ and $Pt_{32}Fe_{68}$ NWs (in acetic acid at 70 °C) showed the removal of some Fe in PtFe NWs, forming $Pt_{80}Fe_{20}$ and $Pt_{77}Fe_{23}$, respectively. The alloy with 75% Pt showed a high stability in 0.1 M $HClO_4$ solution.[13] While the remaining surface layer features pure Pt, the subsurface layer is characteristic of bulk Pt_3Fe alloy. The lattice constant of Pt_3Ni NWs was found to be about 2.3% smaller than Pt, and the lattice mismatch was

shown to produce a compressive strain.[29] A PtFe alloy catalyst treated with 0.5 M H_2SO_4 showed a surface compressively strained Pt shell and a lattice-contracted PtFe core, which exhibited enhanced ORR activity.[30] Ultrafine jagged platinum nanowires were shown to exhibit ultrahigh activity for ORR,[31] where the compressive strain was shown to reduce the binding energy of the adsorbent on the densely packed surface, further promoting the activity enhancement. In a study of the surface strain effects on ORR activity[20,32−34] by Strasser and co-workers, the selective electrochemical dissolution was shown to change the composition in the alloy by varying the lattice mismatch (disordered structure) at the interface.[32] The question on whether disordered or ordered alloy structure is beneficial to the improvement of activity and stability after electrochemical dealloying remains elusive, calling for the study of composition and structure in relation to activity and durability, especially under MEA operating condition where some catalysts showed a gradual decrease of activity with potential cycling due to combined effect of metal leaching, diminished atomic-level strain and restructuring of the alloys.[35]

There is a clear need to determine the factors affecting the activity and stability in complex environments. One of the main complexities in many previous studies involved surface surfactant species on the as-synthesized nanoparticles or nanowires and subsequent removal. Using *N,N*-dimethylformamide (DMF) as a solvent in a surfactant-free system,[27,36] we synthesized surfactant-free twisty PtFe NW catalysts in a one-step hydrothermal method with a yield of more than 90%. We employed in situ/operando HE-XRD/PDF and EDS techniques to study the activity and durability under MEA operating
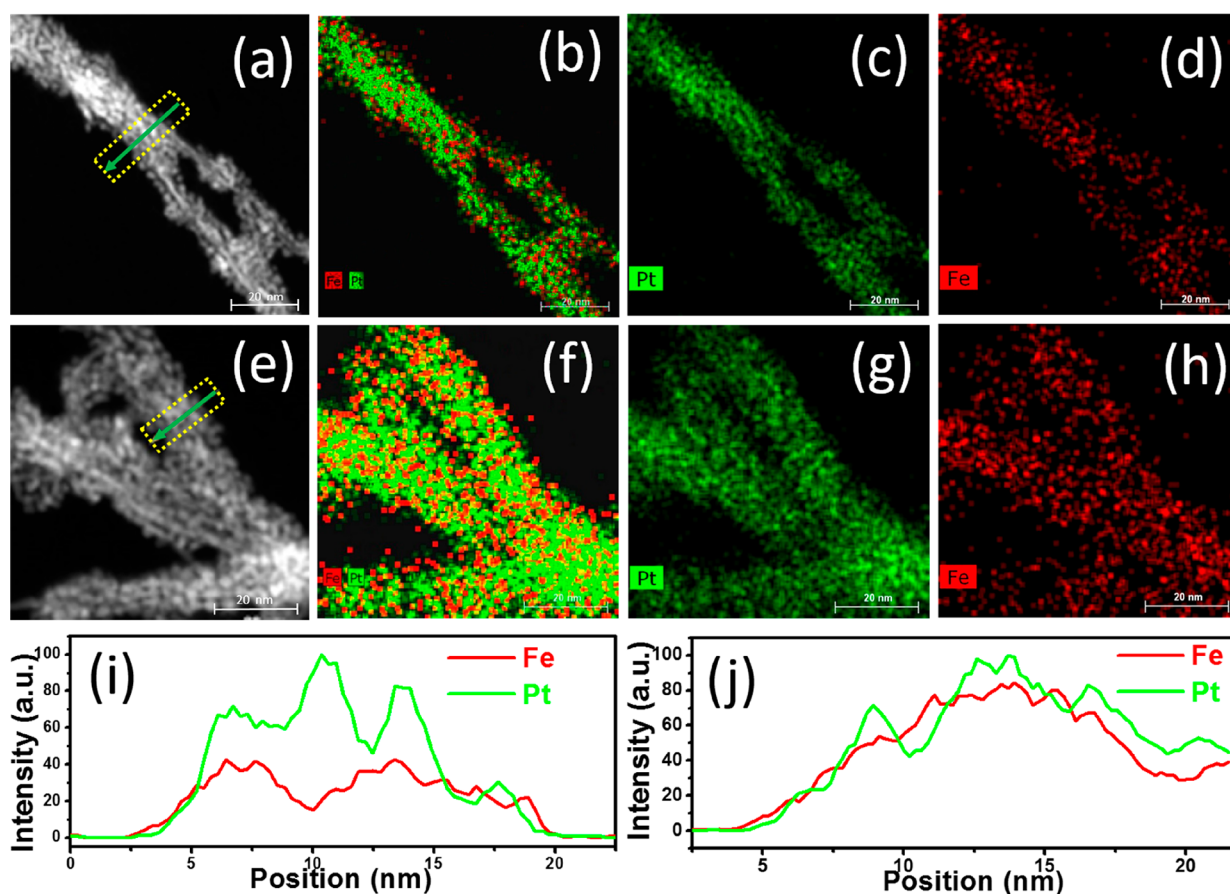
Figure 2. HAADF-STEM images (a, e), EDS overlap images (b, f) and EDS elemental mapping images of Pt (c, g) and Fe (d, h) of $Pt_{42}Fe_{58}$ (a−d) and $Pt_{24}Fe_{76}$ (e−h) NWs, respectively, and EDS line profiles of $Pt_{42}Fe_{58}$ (i) and $Pt_{24}Fe_{76}$ (j) NWs correspond to the green lines in images (a, e), respectively. (Data were collected using Titan G2 60-300 instrument.)

condition, and Monte Carlo 3D modeling to analyze the atomic ordering, disordering, lattice strain, and metal coordination number and distribution. In comparison with smooth and ultrathin (∼2.5 nm) NWs[28] and high-index faceted Pt skinned rough PtFe NWs (∼25 nm),[37] our as-synthesized twisty NWs (∼16 nm) with less than 25% Pt are shown to exhibit the highest initial mass activity (2.9 A/mg$_{Pt}$) and a high durability (up to 120 000 cycles in accelerated durability test (ADT)) under ORR and fuel cell operating conditions upon reaching the final alloy composition and lattice strain.

2. RESULTS AND DISCUSSION

2.1. Morphologies and Compositions. The as-synthesized $Pt_{24}Fe_{76}$ (Figure 1a−c), $Pt_{42}Fe_{58}$ (Figure 1d−f), and $Pt_{71}Fe_{29}$ (Figure 1g−i) nanowires feature twisty and spiral morphologies, which appear to be formed by connecting with growing nanoparticles in 1D direction (Figure 1). The NWs also appear to exhibit many twists and turns, along with some subnanopores (see Figure S1).

The average width of $Pt_{24}Fe_{76}$ and $Pt_{42}Fe_{58}$ is around 15 nm. Rough surface arrangements of the low-Pt-content NWs are observed, showing growth of twisty particles in various directions on the surface (see Figures 1c,f). Note that rough/irregular surface structures were observed for jagged Pt NWs via electrochemical dealloying, which showed a superior mass activity for ORR (13.6 A/mg$_{Pt}$).[31] In contrast to porous PtFe or PtNi nanowires with rough/irregular surface

atomic arrangement,[38,39] the twisty NW feature is evident for $Pt_{42}Fe_{58}$ (Figure 1a−c) and $Pt_{24}Fe_{76}$ (Figure 1d−f) NWs. In comparison, $Pt_{71}Fe_{29}$ NWs appear less twisty (Figure 1g−i), featuring relatively smooth bundled nanowires.

Samples of $Pt_{71}Fe_{29}$ (Figure S3), $Pt_{42}Fe_{58}$ (Figure 2a−d) and $Pt_{24}Fe_{76}$ (Figure 2e−h) NWs were analyzed by high-angle annular dark-field scanning transmission electron microscopy (HAADF-STEM) and energy dispersive X-ray spectroscopy (EDS) (Figure 2 and Figure S3), revealing a random distribution of Pt and Fe across and along the NWs. As shown in the HAADF-STEM images and their corresponding EDS line scan images (Figure 2), $Pt_{42}Fe_{58}$ (Figure 2i) and $Pt_{24}Fe_{76}$ (Figure 2j) NWs display random element distribution on the surface and across the NW. This observation, in terms of composition distribution, is in fact further substantiated by the experimental HE-XRD/PDF data and 3D structure modeling (see the next subsection).

Based on X-ray diffraction (XRD) patterns (Table S1 and Figure S4A), all fresh NWs, except $Pt_{12}Fe_{88}$ NWs, are fcc-type nanoalloys. The XRD-determined NWs domain size (based on Debye−Scherrer equation) showed little change from $Pt_{24}Fe_{76}$ to $Pt_{71}Fe_{29}$ (Figure S4B). The (111)/(200) facet ratio of Pt_nFe_{100-n} NWs depends on Pt composition and is obviously higher than that of pure Pt NWs (Figure S4C).

2.2. Atomic Nanophase Structure. Using ex situ synchrotron high-energy X-ray diffraction (HE-XRD), atomic pair distribution functions (PDFs) were obtained for fresh NWs of Pt/C and Pt_nFe_{100-n}/C (n = 12, 24, 42, 71, 82). Figure
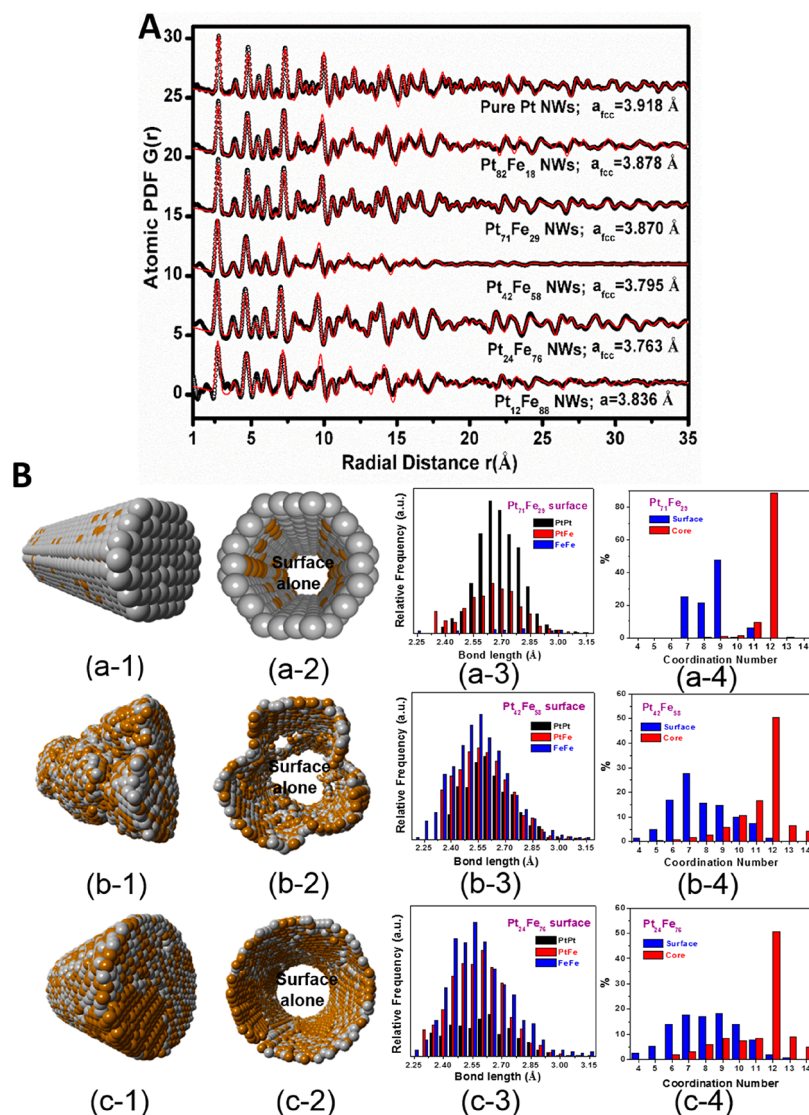
Figure 3. (A) Experimental PDF-fit derived fcc lattice parameters and fcc-model fit to atomic PDFs for NWs of Pt, $Pt_{82}Fe_{18}$, $Pt_{71}Fe_{29}$, $Pt_{42}Fe_{58}$, and $Pt_{24}Fe_{76}$. For $Pt_{12}Fe_{88}$, the model is composed of interpenetrating bcc- and fcc-like nanodomains with an apparent fcc lattice constant. Experimental data (symbols) and fitting data (red lines). The black circles are the data obtained from HE-XRD, while the red lines were calculated from the 3D models. (B) Images of the models for the NWs of $Pt_{71}Fe_{29}$, $Pt_{42}Fe_{58}$, and $Pt_{24}Fe_{76}$, showing all the atoms (a-1), (b-1), and (c-1), the atoms at the surface (a-2), (b-2), and (c-2), the distribution of the interatomic bond distances at the surface: Pt−Pt, Pt−Fe, and Fe−Fe (a-3), (b-3), and (c-3)), and the distribution of the coordination numbers in the core and at the surface: (a-4), (b-4), and (c-4). The distribution of the interatomic bond distances in the core is shown in Figure S7.

3A show the experimental PDF data and fcc lattice parameters for the TNWs derived from a crystallography-constrained modeling. The apparent fcc lattice constants are shown by the respective PDF data sets. The plot of the lattice constant for Pt_nFe_{100-n} TNWs (see Figure S5) shows a minimum for $n =$ 24%. The NWs are in well-alloyed state, and the evolution of lattice constants with the bimetallic composition follows Vegard's law. For $Pt_{12}Fe_{88}$ NWs, there is an increased Fe segregation in the NWs (see Figure S4A).

As shown by the total PDFs in Figure 3A, $Pt_{71}Fe_{29}$, $Pt_{42}Fe_{58}$, and $Pt_{24}Fe_{76}$ NWs exhibit a well-ordered atomic structure. In particular, $Pt_{71}Fe_{29}$ and $Pt_{24}Fe_{76}$ TNWs show long-range correlation (LRC), whereas PDF of $Pt_{42}Fe_{58}$ shows short-range correlation (SRC) only as indicated by the higher-r oscillations in the respective PDF data sets. LRC cannot be achieved with small domains randomly oriented in the NWs. The LRC of $Pt_{24}Fe_{76}$ suggests an extensive structural order.

With the Fe content increasing, the lattice mismatch could not be neglected, regardless of the LRC or SRC structure. To gain an insight into the detailed domain structures, 3D modeling with the 3D models refined against the PDF data was performed. Figure 3B shows 3D models for the NWs with different compositions (see also Figure S6).

Considering the less twisty NWs with more NW-bundling feature, $Pt_{71}Fe_{29}$ NWs were modeled as a single thin NW with a uniform diameter of 2.5 nm. Figure 3B-a-1 shows the model of a smooth single NW, and Figure 3B-a-2 shows the morphology of surface first atomic layer. The starting point was a single cut out of the ordered fcc phase of Pt_3Fe. Some substitutional Fe was then randomly introduced while keeping at the surface mostly Pt. From the initial model, the normal procedure was to carry out some relaxation using semi-empirical potentials and the reverse Monte Carlo refinement. The resulting model reproduces very well the data, which is

Table 1. Summary of 3D Modeling Results for the PtFe NWs

Pt_xFe_y	MA (A/mg_{Pt})	lattice constant	lattice strain (%)	Pt−Pt (Å) (mean)	Pt−Pt (Å) (surface)	CN (total)	CN (Pt−Pt) (surface)	CN (Pt−Fe)
24:76	2.9	3.763	−4.2	2.658	2.602	8.7	2.5	6.2
42:58	2.3	3.795	−3.6	2.674	2.617	8.6	4.0	4.6
71:29	1.4	3.869	−1.5	2.734	2.692	8.4	7.3	1.0
100:0	0.3	3.918						

essentially the PDF of the fcc structure attenuated according to the shape (see Figure 3A). Figure 3B-a-3 shows the distribution of the interatomic bond distances at the surface for Pt−Pt, Pt−Fe and Fe−Fe pairs. The total mean value is 2.734 Å, corresponding to a lattice constant of 3.867 Å of the fcc structure. However, the atoms at the surface are somewhat compressed, yielding a Pt−Pt bond average of 2.692 Å, i.e., the mean value of black bars in Figure 3B-a-3. Similarly, the interatomic bond distances in the core show subtle differences in relative distribution (Figure S7). Figure 3B-a-4 shows the distribution of the coordination numbers (CNs) in the core and at the surface, displaying a good structural order in terms of CN. In these cases, Fe−Fe, Pt−Fe, and Pt−Pt bonds are considered but the results are split depending on where the atoms are located: core (red) or surface (blue). The mean CN of the surface atoms is 8.4 for Pt_3Fe model. As shown in Table 1, the CNs, while being model dependent in terms of absolute values, provide us the information for assessing the trends.

The $Pt_{42}Fe_{58}$ NWs were modeled as a domain size of 4.5 nm in diameter (twisty bulb diameter; see Figure 3A), with an initial model composed by quasi-spherical domains randomly oriented (Figure 3B-b-1) and the surface atoms morphology for first layer as shown in Figure 3B-b-2. The STEM-EDS elemental mapping data show an even distribution of the elements for this sample. For this and those samples with lower content of Pt, the Fe−Fe partial PDF obtained from the resonant XRD experiment suggests some existence of bcc structure. According to the phase diagram, iron can be alloyed with Pt keeping the bcc structure up to 15% Pt. Thus, one of the 7 domains in the model is bcc with a higher content of Fe ($0.15\ Pt_{10}Fe_{90}$ (bcc) + $0.85\ Pt_{50}Fe_{50}$ (fcc)). In Figure 3B-b-3, the mean value of the Pt−Pt bond is 2.617 Å at the surface. A total mean bond distance obtained is 2.674 Å. From the coordination numbers (Figure 3B-b-4, and Table 1), the mean CN of the surface atoms is 8.6 for $Pt_{42}Fe_{58}$ model.

For $Pt_{24}Fe_{76}$ NWs with a nonuniform diameter, it is modeled in Figure 3B-c-1 using 2.5 nm average diameter (twisty bulb diameter), with the surface atoms morphology for the first layer as shown in Figure 3B-c-2. The initial model involved a fcc cylindrical matrix and embedded 5 quasi-spherical domains from which 3 domains were bcc with higher content of Fe and represent about 30% of the model ($0.30\ Pt_{10}Fe_{90}$ (bcc, embedded) + $0.25\ Pt_{20}Fe_{80}$ (fcc, embedded) + $0.45\ Pt_{35}Fe_{65}$ (fcc, matrix)). Despite this singular choice, the result looks quite good and the Fe−Fe partial PDF exhibits a slight bcc character, consistent with the experimental data. As shown in Figure 3B-c-3, the total mean bond distance is 2.658 Å. Note that this is a mixture of structural phases, even if it features LRC structure. At the surface the mean value of the Pt−Pt bond is 2.602 Å, and the mean CN of the surface atoms is 8.7 (Figure 3B-c-4 and Table 1).

A distinctive difference of $Pt_{24}Fe_{76}$ NWs (Figure 1c) from $Pt_{42}Fe_{58}$ NWs (Figure 1f) is that the former appears to exhibit more coherently stacked clusters than the latter. This means that the overall twisty $Pt_{24}Fe_{76}$ NW features a coherent-

collection of many smaller particles than $Pt_{42}Fe_{58}$ NW. The nanowire consists of many small domains. There are seven domains for $Pt_{42}Fe_{58}$ and five domains for $Pt_{24}Fe_{76}$ as shown by 3D modeling. The length of structural coherences for $Pt_{42}Fe_{58}$ appears diminished in comparison with $Pt_{71}Fe_{29}$ and $Pt_{24}Fe_{76}$. That is why the smooth/less twisty morphology ($Pt_{71}Fe_{29}$) and the more coherently stacked morphology ($Pt_{24}Fe_{76}$) exhibit LRC character, whereas $Pt_{42}Fe_{58}$ shows SRC character.

In summary, the 3D modeling results show that $Pt_{71}Fe_{29}$ is LRC/ordered fcc phase, while $Pt_{24}Fe_{76}$ and $Pt_{42}Fe_{58}$ feature fcc and bcc mixed phases. $Pt_{71}Fe_{29}$, $Pt_{42}Fe_{58}$, and $Pt_{24}Fe_{76}$ exhibit compressive strains of 1.5%, 3.6%, and 4.2%, respectively. The 1.5% compressive strain for $Pt_{71}Fe_{29}$ (less twisty NWs) is due to the larger percentage of Pt atoms. It is smaller than that for Pt_3Ni alloy NWs because of the different atomic size of Fe and Ni (2.3% compressive strain based on lattice mismatch).[29] A higher degree of lattice mismatch/disordered structure results in larger compressive strain for the alloy NWs. A further increase in the compressive strain is observed with the low-Pt-content twisty NWs, which exhibit some bcc-like structural features. As summarized in Table 1, where the mass activity (MA) will be discussed in the next subsection, it is the combination of the smaller lattice constant, larger lattice strain, shorter Pt−Pt bond distance and smaller coordination number at the surface that determines the electrocatalytic activity. This assessment is based on previous literature reports,[16−18,22,30,34] including our own recent works.[15,35,40,41] In general, the smaller lattice constant, larger lattice strain, and shorter Pt−Pt bond distance is associated with a higher degree of alloying, which would lead to more effective bridge adsorption of O_2 on the active sites of Pt. This, in turn, would weaken more effectively the double bond of O_2. As for the CN at the surface, the decreased Pt−Pt CN is accompanied by an increased Pt−Fe CN. This means a better alloying, which would favor the operation of the synergistic ligand effect of Fe on Pt, enriching electrons for better donation to the π^* orbital of the double bond of adsorbed O_2. This understanding is indeed substantiated by the electrocatalytic properties as discussed next.

2.3. Electrocatalytic Properties. The electrocatalytic activity of the NW catalysts for ORR were examined using cyclic voltammetry (CV) and rotating disk electrode (RDE). Figure 4 shows a representative set of data for Pt_nFe_{100-n} NWs. Electrochemical surface active area (ECSA) was calculated from the CV curves (Figure 4A) and the mass activity (MA) and specific activity (SA) were determined from the RDE curves (Figure 4B). As shown in Figure 4C, MA and SA decrease with Pt% in the catalysts, displaying a maximum at ∼24% Pt (see also Table S2). In contrast, the lattice constant increases with Pt%, displaying a minimum at ∼24% Pt. There is a clear composition dependence of the activity, and the high activity at low Pt percentage in the PtFe NWs is in contrast to the previous report of high activity only for ∼75% Pt in PtFe catalysts.[12,13,37] There is also a clear correlation between the activity and the lattice constant. The higher activity is linked to
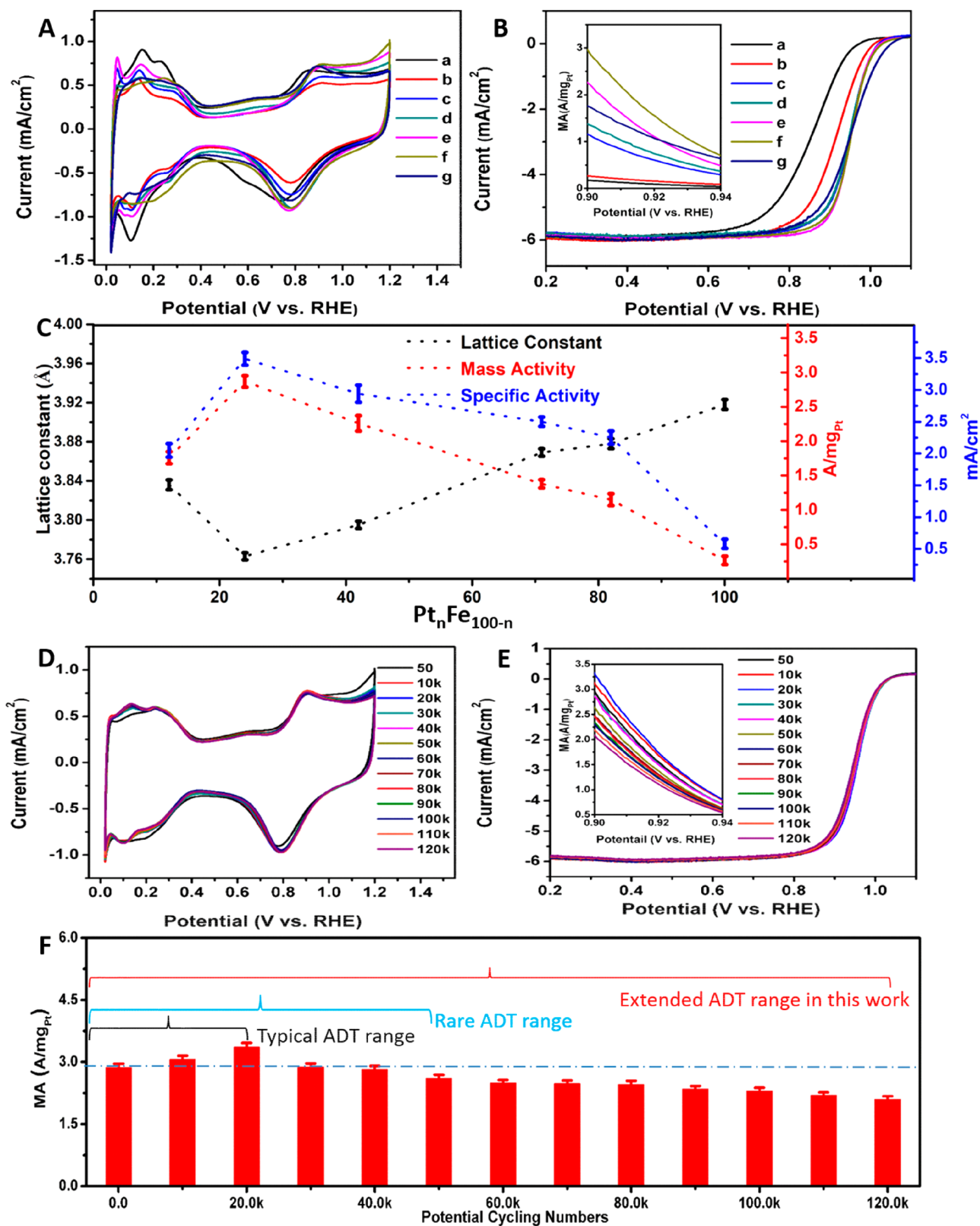
Figure 4. CV (A) and RDE (B) curves of Pt_nFe_{100-n} NWs (Pt NPs (a), Pt (b), $Pt_{82}Fe_{18}$ (c), $Pt_{71}Fe_{29}$ (d), $Pt_{42}Fe_{58}$ (e), $Pt_{24}Fe_{76}$ (f), and $Pt_{12}Fe_{88}$ (g) NWs). Inset in B: MA in the indicated potential range. (C) MA, SA, and lattice constant vs Pt composition in Pt_nFe_{100-n} NWs. Glassy carbon electrode (geometric area 0.196 cm^2): coated with 10 μL of catalyst ink; Electrolyte, 0.1 M $HClO_4$ saturated with high-purity N_2 for CV and saturated with high-purity O_2 for RDE; scan rate: 50 mV/s for CV and 10 mV/s for RDE; Rotation speed: 1600 rpm.(D-E) CV and RDE curves of $Pt_{24}Fe_{76}$ before and after ADT (10 000 to 120 000 cycles). Inset in E: MA in the indicated potential range. (F) MA vs cycle number over $Pt_{24}Fe_{76}$ in ADT. Condition: 25 °C in O_2-saturated 0.1 M $HClO_4$ at 10 mV/s and 1600 rpm.
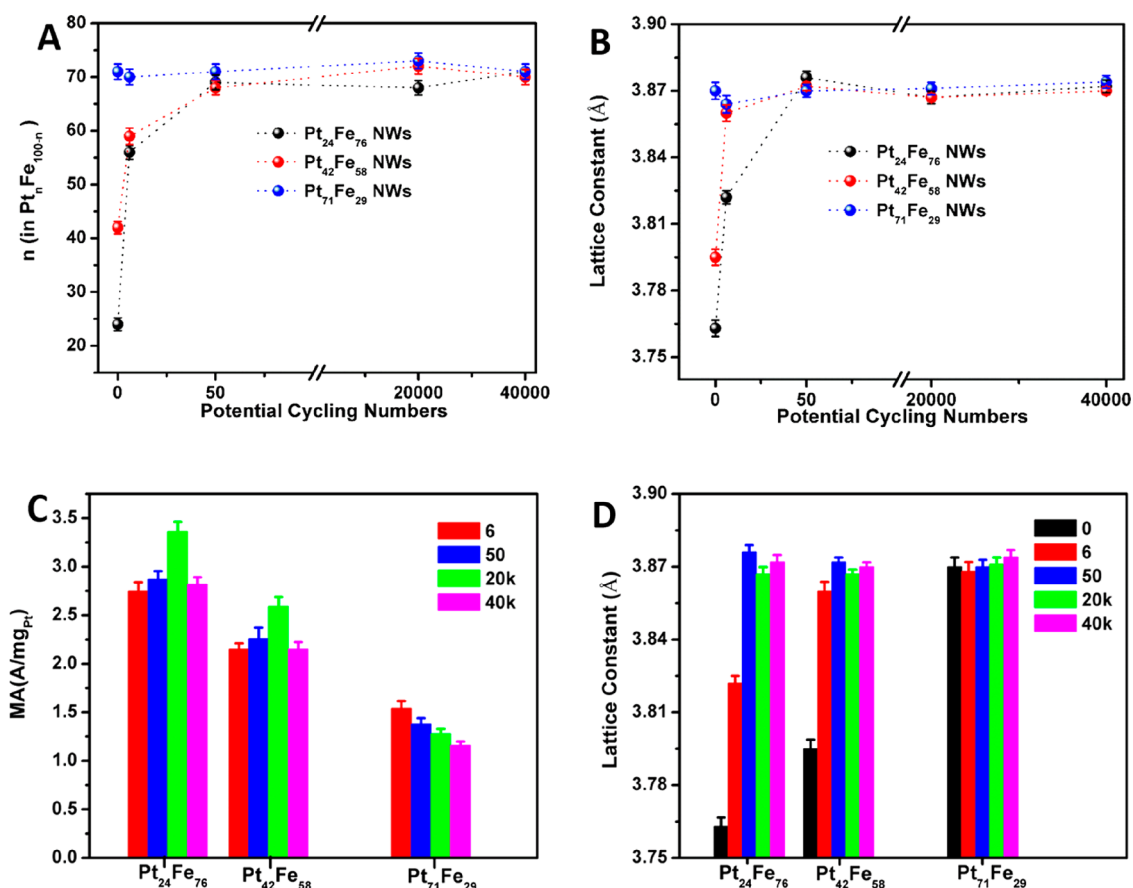
Figure 5. Relationships between Pt(%) (A) and lattice constant (B) and ADT potential cycling numbers for PtFe NWs of different Pt compositions. MA (C) and lattice constant (D) measured after 6, 50, 20k, and 40k cycles in ADT vs the Pt composition in PtFe NWs. Lattice constants for fresh catalysts are also included in D for comparison.

the smaller lattice constant, which is true even though the Pt composition and lattice constant changed during the RDE measurement.

For $Pt_{12}Fe_{88}$, there is a small degree of phase segregation in the NWs (see Figure S4A) with interpenetrating bcc- and fcc-like nanodomains and apparent fcc lattice constant (see Figure 3A). The slightly disordered fcc structure favors a better activity, exhibiting the order of ORR activity: $Pt_{24}Fe_{76}$ > $Pt_{42}Fe_{58}$ > $Pt_{71}Fe_{29}$. Furthermore, the (111)/(200) crystal face ratio of Pt_nFe_{100-n} NWs is shown to be higher than that of pure Pt NWs after initial test (see Figure S4C), indicating that the (111) facets likely played a role in enhancing the catalytic activity. The activity apparently scales with the compressive strain (see Tables 1 and S3). In previous work on $Pt_{45}Fe_{55}$ NPs,[16] a compressive strain of 1.2% was shown to achieve ORR activity of 0.78 A/mg$_{Pt}$. In comparison, our $Pt_{42}Fe_{58}$ NWs show a 3-fold increase in the lattice compression (3.6%), and the ORR activity shows an increase by a factor of 3. Note that there is also sharp difference in Pt–Fe CN (see Table 1), indicating the important role of alloying in our NW catalysts.

Figure 4D shows a typical set of CV curves for $Pt_{24}Fe_{76}$ NWs before and after ADT, from which the calculated ECSA showed only 6% reduction after 120k cycles. In previous work, a decrease of ∼8% after 50k ADT was reported for Pt skin-Pt_3Fe z-NWs,[37] and improved durability without much impact on ECSA was reported for $PtNi_3$ after removing Ni.[42,43] Figure 4E shows RDE curves of twisty $Pt_{24}Fe_{76}$ NWs with ADT cycle numbers up to 120 k cycles, from which calculated MAs show

high activity in the potential range of 0.90−0.94 V (see Figure 4E insert).

As shown in Figure 4F for the MA as a function of cycle numbers over $Pt_{24}Fe_{76}$ NWs up to 120 000 cycles, the activity is shown to remain ∼73% after 120 000 cycles, which is to our knowledge the longest cycle number reported so far. Interestingly, the MA increased to 117% after 20 000 cycles (a typical cycle number reported in the literature). There is a gradual and small decrease starting at 50 000 cycles. The composition was found to reach 70% Pt after 50 cycles and remain unchanged afterward. The best durability performance reported for zigzag PtFe NWs with high−index faceted Pt skin is that the activity remained about 75% after 50,000 cycles.[37] In comparison, our twisty $Pt_{24}Fe_{76}$ NWs showed the highest durability among all PtFe catalysts reported for ORR so far. ADT results of PtFe NW catalysts of other composition, $Pt_{42}Fe_{58}$ and $Pt_{71}Fe_{29}$, were shown to retain 30% Fe during first 40k ADT and exhibit a slight loss of ORR activity after 80k cycles (Table S4 and Figures S8 and S9). The MA showed a change to 115% for $Pt_{42}Fe_{58}$ and 93% for $Pt_{71}Fe_{29}$ after 20 000 cycles. In contrast, the MA of commercial Pt/C decreases significantly throughout the ADT, showing ∼40% after 40 000 cycles (see Table S4 and Figure S10). The activity and durability follow the same order of $Pt_{24}Fe_{76}$ > $Pt_{42}Fe_{58}$ > $Pt_{71}Fe_{29}$.

2.4. Catalyst Composition and Structure after ADT. The composition of the PtFe NW catalysts before and after different stages of ADT was examined by ICP analysis (Figure
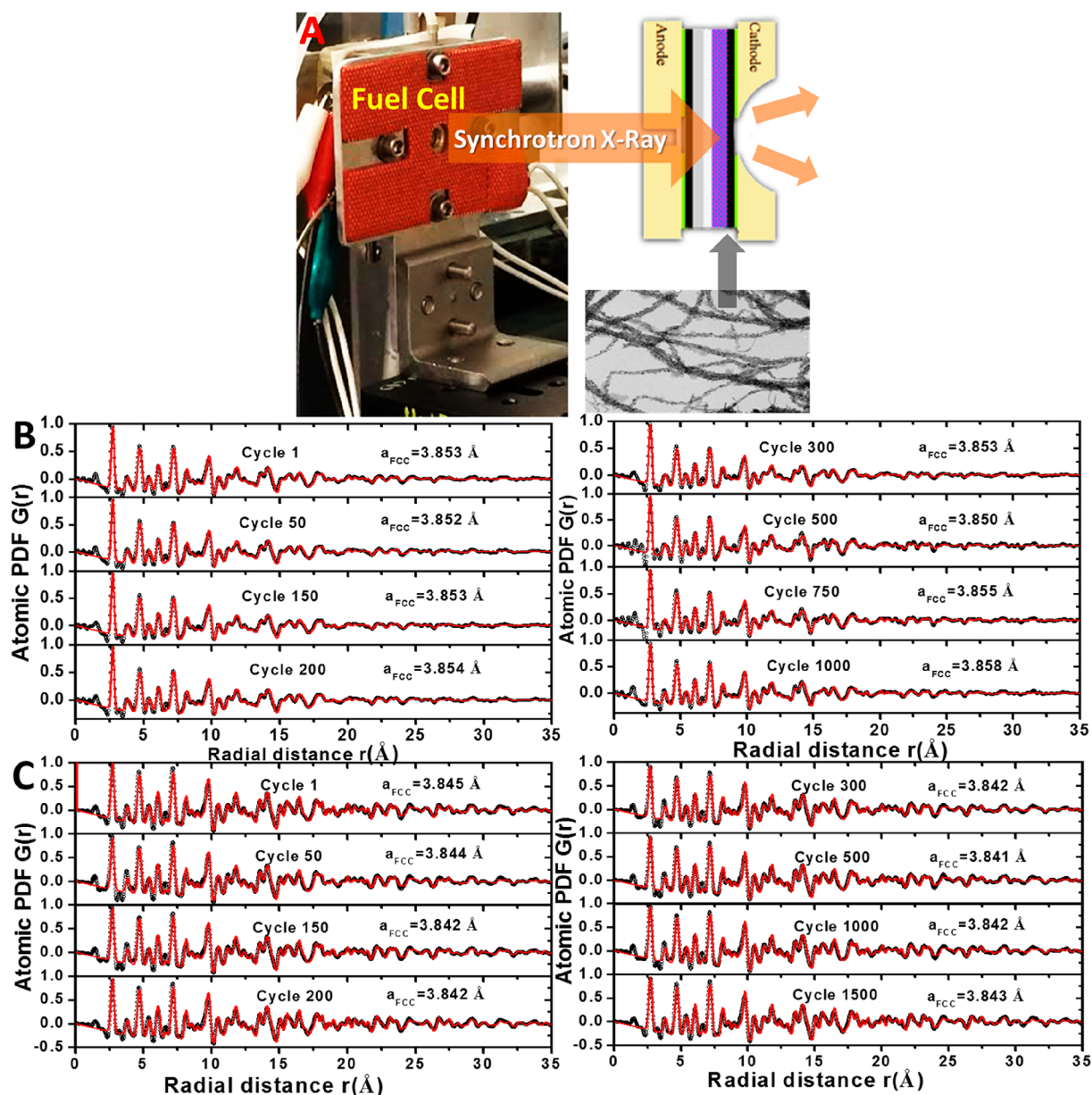
Figure 6. PDFs data derived from synchrotron X-ray HE-XRD data by in situ fuel cell measurements. (A) In situ fuel cell measurement setup. (B and C) Fit to experimental atomic PDFs for $Pt_{42}Fe_{58}$ (B) and $Pt_{24}Fe_{76}$ (C) at different potential cycling numbers up to 1000 or 1500 cycles.

5A and Tables S5A, S5B, and S5C). The Pt composition of $Pt_{71}Fe_{29}$, $Pt_{42}Fe_{58}$ and $Pt_{24}Fe_{76}$ was shown to apparently reach 70% Pt in the bimetallic NWs. The fcc NWs with partial mixed PtFe bcc structure ($Pt_{42}Fe_{58}$ and $Pt_{24}Fe_{76}$) showed a quick leaching of Fe after 40k cycles. In previous work,[13,37] the surface layer of Pt_3Fe featured a Pt skin with the subsurface layer characteristic of bulk Pt_3Fe alloy, and under operating conditions relevant to fuel cells the Pt_3Ni near-surface layer exhibited a compositional oscillation in the Pt-rich outermost and third layers and the Ni-rich second atomic layer.[12] While the stability of the twisty NW catalysts after ADT is in qualitative agreement with the previous works,[12,13,37,44] the composition change is shown to be completed in the first 50 cycles, especially in the first 6 cycles (see Table S6A). It appears that the electrochemical reaction might not play a significant role in the composition change as reported earlier on electrochemical dealloying.[33,45,46] However, the electrochemical reaction was found to play a role in the realloying

process, as supported by the subtle change of compressive strain at 20k cycles and the almost constant composition after 50 cycles (see Table S5).

Data for the lattice constant and ADT potential cycling numbers for PtFe NWs with different Pt content are shown in Figure 5B and Table S5. Interestingly, the trend for the decrease of lattice constant (Figure 5B) is found to be very similar to those for the Pt composition change shown in Figure 5A. In the first 50 cycles (Figure 5C), the MA increase is accompanied by an increase in the ratio of 111/200 (see Table S5). The activity scales with the ratio of 111/200 and the compressive strain (see Table S5). Interestingly, the lattice constants decrease slightly when the compositions reach $Pt_{70}Fe_{30}$ (Figure 5D). The plot for compressive strain vs cycle number displays a maximum at 20k ADT in the range of 50−40k cycles for $Pt_{42}Fe_{58}$ and $Pt_{24}Fe_{76}$, even the composition showed little change after 50 cycles. These findings imply that a realloying process is operative following the initial dealloying
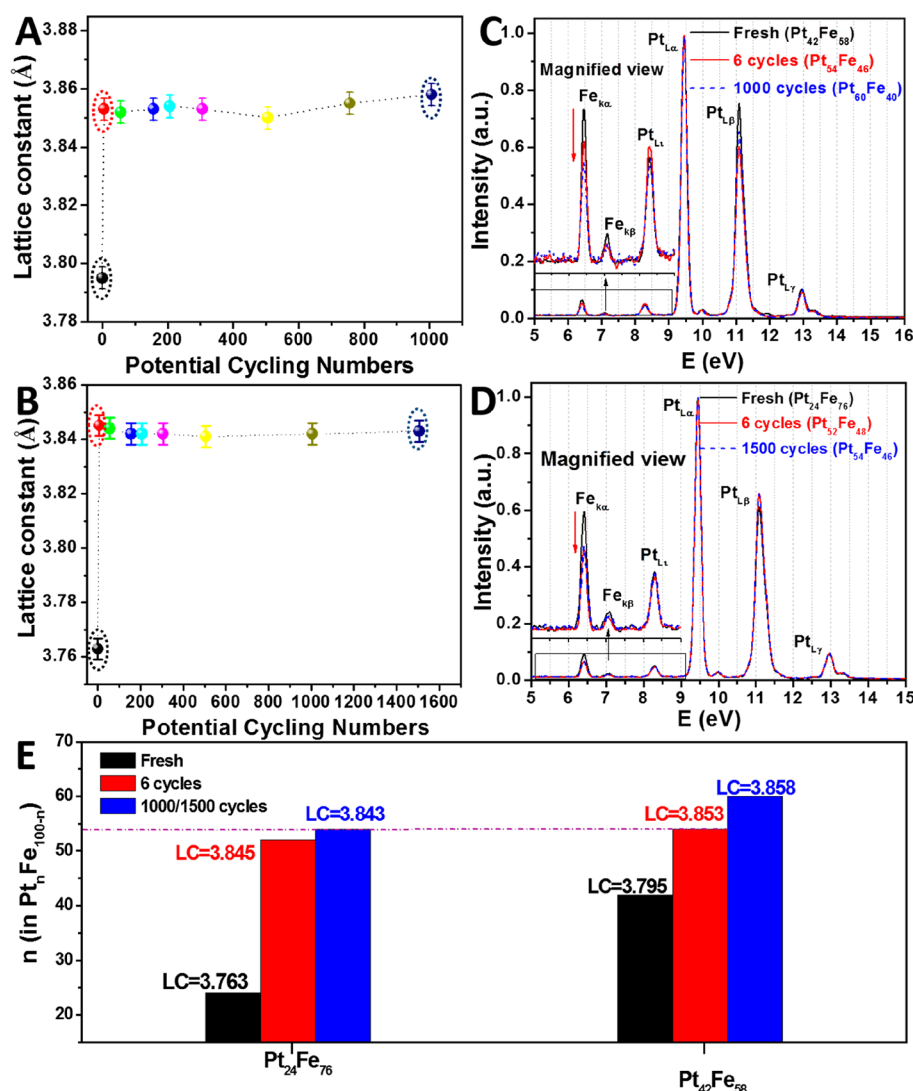
Figure 7. Plots of lattice constants (extracted from in situ HE-XRD/PDF data for $Pt_{42}Fe_{58}$ (A) and $Pt_{24}Fe_{76}$ (B) NWs) vs cycle number. In situ EDX data of $Pt_{42}Fe_{58}$ (C) and $Pt_{24}Fe_{76}$ (D) collected simultaneously. (E) Bar charts comparing lattice constants and compositions of the different catalysts before and after potential cycles (extracted from A to D).

in the first 50 cycles, which increases the compressive strain and contributes to the activity and stability enhancement. Note that there is a subtle increase in the domain size of the catalysts with ADT cycle numbers, especially in the initial 50 cycles (see Figure S11 and Table S5). However, $Pt_{24}Fe_{76}$ and $Pt_{42}Fe_{58}$ TNWs show more stable domain size than that of $Pt_{71}Fe_{29}$ NWs, suggesting their increased resistance to clustering or aggregation propensity in ADT.

Based on the MA data and XRD patterns of three fresh catalysts after ADT (Table S5 and Figure S11), the order of MA matches the order of (111)/(200) ratios throughout the 40k ADT ($Pt_{24}Fe_{76}$> $Pt_{42}Fe_{58}$> $Pt_{71}Fe_{29}$), especially for those after 20k ADT (i.e., 25.6%, 21.4% and −4% change in (111)/(200) ratio, and 17%, 15%, and −7% change in MA after 20k ADT). The increased activity and durability of the twisty NW catalysts are in part due to the increase of (111) facets at given Pt composition and compressive strain, a finding unique for our PtFe NWs. Moreover, considering the jagged/irregular surface atomic arrangement in terms of (100) or (111) facets[31] and surface binding,[47] the twisty morphology of our PtFe NWs ($Pt_{24}Fe_{76}$ and $Pt_{42}Fe_{58}$) should feature more stepped surfaces

or rough/irregular surface atomic arrangements, leading to more compressively strained (111) facets than that of the less twisty $Pt_{71}Fe_{29}$ NWs in ADT and thus higher activity and durability.

As shown by HAADF-STEM and EDS data for $Pt_{24}Fe_{76}$ and $Pt_{71}Fe_{29}$ after 20k ADT (Figure S12), the twisty NWs remain alloy structures. The average diameter size of $Pt_{24}Fe_{76}$ is around 18 nm (Figures S12 and S13), almost the same as the fresh NWs. Considering the attenuated strain and/or ligand effects caused by Co dissolution and counterbalanced by particle growth during voltage cycling reported for other systems,[48] the shortening of the $Pt_{24}Fe_{76}$ twisty nanowires (see Figures S13 and 1) appear to correlate with the increase of mass activity at 20k ADT. In contrast with less twisty $Pt_{71}Fe_{29}$ NWs, the twisty morphology of $Pt_{24}Fe_{76}$ appears to show a distinguished compressive strain during the ADT test, and thus the enhanced activity and durability.

2.5. In Situ HE-XRD and EDS of Catalysts in MEA in Fuel Cell. To reveal the structural and compositional stability of the $Pt_{42}Fe_{58}$ and $Pt_{24}Fe_{76}$. In situ HE-XRD characterizations of the catalysts in a PEM fuel cell were performed (Figure 6A).

Using in situ measurement derived PDFs, the lattice constants for $Pt_{42}Fe_{58}$ and $Pt_{24}Fe_{76}$ were obtained and shown in Figure 6B,C.

The plots of lattice constants (Figure 7A,B) for $Pt_{42}Fe_{58}$ and $Pt_{24}Fe_{76}$ were obtained from Figure 6B,C separately, revealing their changes with the potential cycling number. The lattice constants are found to increase by 1.7% and 2.1% in comparison with that of the ex situ fresh $Pt_{42}Fe_{58}$ and $Pt_{24}Fe_{76}$. Surprisingly, the lattice constant dramatically increases in the first 6 cycles (the lattice constants are 3.853 and 3.845 Å after 6 potential cycles) and then fluctuated slightly in the following 1000/1500 cycles from 3.853 to 3.858 Å and from 3.845 to 3.842 Å for $Pt_{42}Fe_{58}$ and $Pt_{24}Fe_{76}$ separately, throughout 1000/1500 cycles in the in situ experiment. Figure 7C,D show the ex situ and in situ EDX of $Pt_{42}Fe_{58}$ and $Pt_{24}Fe_{76}$, indicating that the compositions changed slightly (also see Table S6B) from $Pt_{54}Fe_{46}$ (6 cycles) to $Pt_{60}Fe_{40}$ (1000 cycles) and from $Pt_{52}Fe_{48}$ (6 cycles) to $Pt_{54}Fe_{46}$ (1500 cycles) for fresh $Pt_{42}Fe_{58}$ and $Pt_{24}Fe_{76}$ NWs, respectively. It is evident that the lattice constant/structure and composition of $Pt_{24}Fe_{76}$ NWs are super stability throughout the 1000/1500 cycles in the fuel cell after the first 6 cycles. Interestingly, there is a propensity of evolution of the mixed fcc and bcc structures for the twisty NWs to a single fcc structure as revealed by comparing the ex-situ and in situ HE-XRD/PDF results. The stable (111) facet of fcc structure[26] is also known to enhance the stability of NWs.

In comparison with that of other MEA tests reported for state-of-the-art catalysts in in situ fuel cell experiments,[49−51] our twisty $Pt_{24}Fe_{76}$ NWs in situ fuel cell experiments show the most stable feature in terms of composition and the lattice constant (see Table S7).[25,35,40,49−51] Based on the recent literature reports on using Fe-based catalysts in PEMFC,[52] use of catalysts with lower iron loading (0.5 wt % Fe loading) mitigates the Fenton reaction which hurts the fuel cell film. We showed that use of $Pt_{71}Fe_{29}$, indeed, did not release iron (see Figure 5A). Also, the fuel cell testing cycles (<1500) would not have a significant Fenton reaction as supported by the similarity of the catalysts with higher iron content within the in situ experiment time range.

Interestingly, the low-Pt twisty $Pt_{24}Fe_{76}$ NWs exhibited a lattice constant smaller than that for the high-Pt twisty NWs though the compositions are practically the same after Fe dealloying. For example, the lattice constants are 3.843 and 3.853 Å for $Pt_{24}Fe_{76}$ and $Pt_{42}Fe_{58}$ when the compositions are $Pt_{54}Fe_{46}$ after dealloying (see Figure 7E). This could explain the observation that the low-Pt PtFe NWs have a higher activity than that of high-Pt PtFe NWs due to the low lattice constant/high compressive strain. Combing with the 3D model for $Pt_{42}Fe_{58}$ and $Pt_{24}Fe_{76}$ alloy catalysts, we first find that the alloy catalyst with more Fe atoms in the inner core ($Pt_{24}Fe_{76}$) exhibits more stable composition and lattice constant/structure in the in situ MEA test, consistent with earlier report for Ni enriched inner shell.[44]

To assess the stability of $Pt_{42}Fe_{58}$ and $Pt_{24}Fe_{76}$ NWs, the electrochemical characteristics of the catalysts in the in situ fuel cell was also examined (see Figure S14), which was similar to performance test of other alloy catalysts with different compositions and morphologies.[53] The relative ECSA values (calculated by integrating the PtO reduction charges) showed a slight increase (105% after 1000 cycles for $Pt_{42}Fe_{58}$ (Figure S14A)) or decrease (~4% decrease after 1500 cycles for

$Pt_{24}Fe_{76}$ (Figure S14B)), suggesting that ECSA remains basically unchanged for the twisty NWs.

The $Pt_{42}Fe_{58}$ and $Pt_{24}Fe_{76}$ MEA samples were also examined by using ex-situ XRD/ICP after the in situ experiment, including the background XRD patterns of carbon paper covered with dry Nafion for a comparison (see Figure S15). The final ICP compositions for $Pt_{42}Fe_{58}$ and $Pt_{24}Fe_{76}$ after the in situ experiment are $Pt_{61}Fe_{39}$ and $Pt_{55}Fe_{45}$, respectively. The XRD patterns show that the catalysts have an alloy structure after the in situ HE-XRD, suggesting that the twisty Pt_nFe_{100-n} catalysts are always in alloy phase state throughout the in situ experiment. Also, as reflected by the disappearance of the overlap of (111) and (200) peaks in XRD patterns, the increased crystallinity contributes not only to the improved mechanical strength and heat resistance performance, but also the enhanced mass activity.[31] For $Pt_{24}Fe_{76}$ NWs, the composition is changed to $Pt_{70}Fe_{30}$ after the initial dealloying of Fe. It is the subsequent realloying of the remaining components that enabled the high durability of the catalyst. Moreover, the (111) facet enhancement, accompanied by transformation of the disordered structure to ordered structure and the evolution of the mixed fcc and bcc structure to a single fcc structure (see Figures 3, 6, 7, and S15 and Table S5), also contributed to the high durability, which is in agreement with previous reports about (111) and (200) facet growth and phase change.[4,33,54] In the fuel cell, the composition change from $Pt_{24}Fe_{76}$ to $Pt_{54}Fe_{46}$ in 1500 cycles due to the initial dealloying is consistent with the composition change in RDE but at a slower speed. Realloying of the remaining components played an important role in the enhanced durability.

Overall, the PtFe twisty alloy NWs with mixed PtFe bcc structure, after Fe dealloying in the initial stage, are shown to end up with a stable composition and lattice parameter. The twisty $Pt_{24}Fe_{76}$ NWs, with Fe rich alloy core, shows the most stable feature in terms of composition and the lattice constant for the catalysts reported for in situ fuel cell experiments (see Table S7).[25,35,40,49−51] The low-Pt PtFe NWs maintain a relatively lower lattice constant and higher (111) facets than the high-Pt PtFe NWs, given the same final composition under ORR and fuel cell operating condition. The inner core also played a key role in maintaining the lattice strain and thus the catalyst activity and durability.

3. CONCLUSIONS

In conclusion, we show the first example of highly efficient synthesis of the twisty nanowire shaped platinum−iron alloy catalysts by a simple one-step surfactant-free hydrothermal method. We have also demonstrated that the catalyst with an optimal composition of ~24% Pt as prepared exhibit the highest mass activity, which is ~20 times higher than that of commercial Pt catalyst, and the highest durability, which displays less than 2% loss of activity after 40 000 cycles and less than 30% loss after 120 000 cycles. These are the highest activity and longest durability among all PtFe-based nano-catalysts under ORR or fuel cell operating conditions reported so far. The twisty PtFe NWs are shown to remain alloy state despite the propensity of dealloying under the ORR and fuel cell operating conditions, as evidenced by unchanged twisty morphology and the lattice strain after the initial dealloying process. The structural origin of the enhanced activity and durability is further substantiated by HE-XRD/PDF analysis and 3D modeling of the lattice constant and metal coordination across the nanostructure. The activity strongly

depends on the composition of the as-synthesized catalysts and this dependence remains unchanged despite the evolution of the composition of the different catalysts and their lattice constants under ORR or fuel cell operating conditions toward a single composition (70% Pt under ORR or 55% under fuel cell operating conditions) and a single fcc lattice constant (0.387 nm). While dealloying under fuel cell operating condition starts at phase-segregated domain sites leading to a final fcc alloy structure with subtle differences in surface morphology, the combination of realloying and TNW morphology is shown to play a key role in maintaining the surface lattice strain and faceting, which is responsible for the origin of the high activity and durability enhancement and the sintering resistance. These findings have provided detailed structural insights into the enhanced activity and durability of the PtFe nanowire catalysts, and also highlighted the importance of the composition tunability and realloying process for achieving highly active and durable low-Pt-content alloy catalysts for fuel cell applications.

■ ASSOCIATED CONTENT

Ⓢ Supporting Information

The Supporting Information is available free of charge at https://pubs.acs.org/doi/10.1021/jacs.9b10239.

Additional experimental data include TEM/SEM, XRD of fresh Pt_nFe_{100-n} NWs, ex situ XRD data after different ADT from RDE/in situ fuel cell experiments, ECSA data of in in situ fuel cell, ICP data, in situ EDX data, 3D modeling results, and fuel cell test results (PDF)

■ AUTHOR INFORMATION

Corresponding Authors

Gang Yu − *Hunan University, Changsha, China;* ⓞ orcid.org/0000-0002-3184-9045; Email: yuganghnu@163.com

Valeri Petkov − *Central Michigan University, Mt. Pleasant, Michigan;* ⓞ orcid.org/0000-0002-6392-7589; Email: petko1vg@cmich.edu

Chuan-Jian Zhong − *State University of New York at Binghamton, Binghamton, New York;* ⓞ orcid.org/0000-0003-0746-250X; Email: cjzhong@binghamton.edu

Other Authors

Zhijie Kong − *Hunan University, Changsha, China, and State University of New York at Binghamton, Binghamton, New York*

Yazan Maswadeh − *Central Michigan University, Mt. Pleasant, Michigan*

Jorge A. Vargas − *Central Michigan University, Mt. Pleasant, Michigan*

Shiyao Shan − *State University of New York at Binghamton, Binghamton, New York*

Zhi-Peng Wu − *State University of New York at Binghamton, Binghamton, New York;* ⓞ orcid.org/0000-0002-5422-1349

Haval Kareem − *CCDC Army Research Laboratory, Adelphi, Maryland*

Asher C. Leff − *CCDC Army Research Laboratory, Adelphi, Maryland*

Dat T. Tran − *CCDC Army Research Laboratory, Adelphi, Maryland*

Fangfang Chang − *State University of New York at Binghamton, Binghamton, New York*

Shan Yan − *State University of New York at Binghamton, Binghamton, New York*

Sanghyun Nam − *State University of New York at Binghamton, Binghamton, New York*

Xingfang Zhao − *State University of New York at Binghamton, Binghamton, New York*

Jason M. Lee − *State University of New York at Binghamton, Binghamton, New York*

Jin Luo − *State University of New York at Binghamton, Binghamton, New York;* ⓞ orcid.org/0000-0002-4363-8886

Sarvjit Shastri − *Argonne National Laboratory, Argonne, Illinois*

Complete contact information is available at:
https://pubs.acs.org/10.1021/jacs.9b10239

Notes
The authors declare no competing financial interest.

■ ACKNOWLEDGMENTS

■ REFERENCES

(1) Li, K.; Li, X.; Huang, H.; Luo, L.; Li, X.; Yan, X.; Ma, C.; Si, R.; Yang, J.; Zeng, J. One-Nanometer-Thick PtNiRh Trimetallic Nanowires with Enhanced Oxygen Reduction Electrocatalysis in Acid Media: Integrating Multiple Advantages into One Catalyst. *J. Am. Chem. Soc.* **2018**, *140*, 16159.

(2) Chen, C.; Kang, Y.; Huo, Z.; Zhu, Z.; Huang, W.; Xin, H. L.; Snyder, J. D.; Li, D.; Herron, J. A.; Mavrikakis, M.; Chi, M.; More, K. L.; Li, Y.; Markovic, N. M.; Somorjai, G. A.; Yang, P.; Stamenkovic, V. R. Highly Crystalline Multimetallic Nanoframes with Three-Dimensional Electrocatalytic Surfaces. *Science* **2014**, *343*, 1339.

(3) Zhang, L.; Roling, L. T.; Wang, X.; Vara, M.; Chi, M.; Liu, J.; Choi, S. I.; Park, J.; Herron, J. A.; Xie, Z.; Mavrikakis, M.; Xia, Y. Platinum-based nanocages with subnanometer-thick walls and well-defined, controllable facets. *Science* **2015**, *349*, 412.

(4) Niu, Z.; Becknell, N.; Yu, Y.; Kim, D.; Chen, C.; Kornienko, N.; Somorjai, G. A.; Yang, P. Anisotropic phase segregation and migration of Pt in nanocrystals en route to nanoframe catalysts. *Nat. Mater.* **2016**, *15*, 1188.

(5) Lim, B.; Jiang, M.; Camargo, P. H.; Cho, E. C.; Tao, J.; Lu, X.; Zhu, Y.; Xia, Y. Pd-Pt Bimetallic Nanodendrites with High Activity for Oxygen Reduction. *Science* **2009**, *324*, 1302.

(6) Wang, D.; Li, Y. Bimetallic Nanocrystals: Liquid-Phase Synthesis and Catalytic Applications. *Adv. Mater.* **2011**, *23*, 1044.

(7) Li, L.; Liu, H.; Wang, L.; Yue, S.; Tong, X.; Zaliznyak, T.; Taylor, G. T.; Wong, S. S. Chemical Strategies for Enhancing Activity and Charge Transfer in Ultrathin Pt Nanowires Immobilized onto Nanotube Supports for the Oxygen Reduction Reaction. *ACS Appl. Mater. Interfaces* **2016**, *8*, 34280.

(8) Liu, H.; An, W.; Li, Y.; Frenkel, A. I.; Sasaki, K.; Koenigsmann, C.; Su, D.; Anderson, R. M.; Crooks, R. M.; Adzic, R. R.; Liu, P.; Wong, S. S. In Situ Probing of the Active Site Geometry of Ultrathin Nanowires for the Oxygen Reduction Reaction. *J. Am. Chem. Soc.* **2015**, *137*, 12597.

(9) Koenigsmann, C.; Santulli, A. C.; Gong, K.; Vukmirovic, M. B.; Zhou, W. P.; Sutter, E.; Wong, S. S.; Adzic, R. R. Enhanced Electrocatalytic Performance of Processed, Ultrathin, Supported Pd—Pt Core—Shell Nanowire Catalysts for the Oxygen Reduction Reaction. *J. Am. Chem. Soc.* **2011**, *133*, 9783.

(10) Lin, R.; Cai, X.; Zeng, H.; Yu, Z. Stability of High-Performance Pt-Based Catalysts for Oxygen Reduction Reactions. *Adv. Mater.* **2018**, *30*, 1705332.

(11) Guedes-Sobrinho, D.; Nomiyama, R. K.; Chaves, A. S.; Piotrowski, M. J.; Da Silva, J. L. F. Structure, Electronic, and Magnetic Properties of Binary Pt_nTM_{55-n} (TM = Fe, Co, Ni, Cu, Zn) Nanoclusters: A Density Functional Theory Investigation. *J. Phys. Chem. C* **2015**, *119*, 15669.

(12) Stamenkovic, V. R.; Fowler, B.; Mun, B. S.; Wang, G.; Ross, P. N.; Lucas, C. A.; Markovic, N. M. Improved Oxygen Reduction Activity on Pt3Ni(111) via Increased Surface Site Availability. *Science* **2007**, *315*, 493.

(13) Stamenkovic, V. R.; Mun, B. S.; Arenz, M.; Mayrhofer, K. J.; Lucas, C. A.; Wang, G.; Ross, P. N.; Markovic, N. M. Trends in electrocatalysis on extended and nanoscale Pt-bimetallic alloy surfaces. *Nat. Mater.* **2007**, *6*, 241.

(14) Du, X. X.; He, Y.; Wang, X. X.; Wang, J. N. Fine-grained and fully ordered intermetallic PtFe catalysts with largely enhanced catalytic activity and durability. *Energy Environ. Sci.* **2016**, *9*, 2623.

(15) Petkov, V.; Prasai, B.; Shastri, S.; Park, H. U.; Kwon, Y. U.; Skumryev, V. Ensemble averaged structure-function relationship for nanocrystals: effective superparamagnetic Fe clusters with catalytically active Pt skin. *Nanoscale* **2017**, *9*, 15505.

(16) Jang, J. H.; Lee, E.; Park, J.; Kim, G.; Hong, S.; Kwon, Y. U. Rational syntheses of core-shell $Fe_x@Pt$ nanoparticles for the study of electrocatalytic oxygen reduction reaction. *Sci. Rep.* **2013**, *3*, 2872.

(17) Wu, Z.; Zhang, W.; Sun, S. Mechanisms for oxygen reduction reactions on Pt-rich and Pt-poor PtFe alloys as the fuel cell cathode. *Comput. Mater. Sci.* **2016**, *125*, 278.

(18) Jia, Q.; Liang, W.; Bates, M. K.; Mani, P.; Lee, W.; Mukerjee, S. Activity Descriptor Identification for Oxygen Reduction on Platinum-Based Bimetallic Nanoparticles: *In Situ* Observation of the Linear Composition—Strain—Activity Relationship. *ACS Nano* **2015**, *9*, 387.

(19) Kobayashi, S.; Wakisaka, M.; Tryk, D. A.; Iiyama, A.; Uchida, H. Effect of Alloy Composition and Crystal Face of Pt-Skin/$Pt_{100-x}Co_x$ [(111), (100), and (110)] Single Crystal Electrodes on the Oxygen Reduction Reaction Activity. *J. Phys. Chem. C* **2017**, *121*, 11234.

(20) Gan, L.; Heggen, M.; O'Malley, R.; Theobald, B.; Strasser, P. Understanding and Controlling Nanoporosity Formation for Improving the Stability of Bimetallic Fuel Cell Catalysts. *Nano Lett.* **2013**, *13*, 1131.

(21) Wang, D.; Yu, Y.; Zhu, J.; Liu, S.; Muller, D. A.; Abruna, H. D. Morphology and Activity Tuning of Cu3Pt/C Ordered Intermetallic Nanoparticles by Selective Electrochemical Dealloying. *Nano Lett.* **2015**, *15*, 1343.

(22) Jia, Q.; Li, J.; Caldwell, K.; Ramaker, D. E.; Ziegelbauer, J. M.; Kukreja, R. S.; Kongkanand, A.; Mukerjee, S. Circumventing Metal Dissolution Induced Degradation of Pt-Alloy Catalysts in Proton Exchange Membrane Fuel Cells: Revealing the Asymmetric Volcano Nature of Redox Catalysis. *ACS Catal.* **2016**, *6*, 928.

(23) Lai, J.; Huang, B.; Tang, Y.; Lin, F.; Zhou, P.; Chen, X.; Sun, Y.; Lv, F.; Guo, S. Barrier-free Interface Electron Transfer on PtFe-Fe2C Janus-like Nanoparticles Boosts Oxygen Catalysis. *Chem.* **2018**, *4*, 1153.

(24) Li, Q.; Wu, L.; Wu, G.; Su, D.; Lv, H.; Zhang, S.; Zhu, W.; Casimir, A.; Zhu, H.; Mendoza-Garcia, A.; Sun, S. New Approach to Fully Ordered fct-FePt Nanoparticles for Much Enhanced Electrocatalysis in Acid. *Nano Lett.* **2015**, *15*, 2468.

(25) Li, J.; Xi, Z.; Pan, Y. T.; Spendelow, J. S.; Duchesne, P. N.; Su, D.; Li, Q.; Yu, C.; Yin, Z.; Shen, B.; Kim, Y. S.; Zhang, P.; Sun, S. Fe Stabilization by Intermetallic $L1_0$-FePt and Pt Catalysis Enhancement in $L1_0$-FePt/Pt Nanoparticles for Efficient Oxygen Reduction Reaction in Fuel Cells. *J. Am. Chem. Soc.* **2018**, *140*, 2926.

(26) Jiang, K.; Zhao, D.; Guo, S.; Zhang, X.; Zhu, X.; Guo, J.; Lu, G.; Huang, X. Efficient oxygen reduction catalysis by subnanometer Pt alloy nanowires. *Sci. Adv.* **2017**, *3*, No. e1601705.

(27) Chang, F.; Shan, S.; Petkov, V.; Skeete, Z.; Lu, A.; Ravid, J.; Wu, J.; Luo, J.; Yu, G.; Ren, Y.; Zhong, C. J. Composition Tunability and (111)-Dominant Facets of Ultrathin Platinum—Gold Alloy Nanowires toward Enhanced Electrocatalysis. *J. Am. Chem. Soc.* **2016**, *138*, 12166.

(28) Guo, S.; Li, D.; Zhu, H.; Zhang, S.; Markovic, N. M.; Stamenkovic, V. R.; Sun, S. FePt and CoPt Nanowires as Efficient Catalysts for the Oxygen Reduction Reaction. *Angew. Chem., Int. Ed.* **2013**, *52*, 3465.

(29) Bu, L.; Ding, J.; Guo, S.; Zhang, X.; Su, D.; Zhu, X.; Yao, J.; Guo, J.; Lu, G.; Huang, X. A General Method for Multimetallic Platinum Alloy Nanowires as Highly Active and Stable Oxygen Reduction Catalysts. *Adv. Mater.* **2015**, *27*, 7204.

(30) Gan, L.; Yu, R.; Luo, J.; Cheng, Z.; Zhu, J. Lattice Strain Distributions in Individual Dealloyed Pt—Fe Catalyst Nanoparticles. *J. Phys. Chem. Lett.* **2012**, *3*, 934.

(31) Li, M.; Zhao, Z.; Cheng, T.; Fortunelli, A.; Chen, C. Y.; Yu, R.; Zhang, Q.; Gu, L.; Merinov, B. V.; Lin, Z.; Zhu, E.; Yu, T.; Jia, Q.; Guo, J.; Zhang, L.; Goddard, W. A., 3rd; Huang, Y.; Duan, X. Ultrafine jagged platinum nanowires enable ultrahigh mass activity for the oxygen reduction reaction. *Science* **2016**, *354*, 1414.

(32) Koh, S.; Strasser, P. Electrocatalysis on Bimetallic Surfaces: Modifying Catalytic Reactivity for Oxygen Reduction by Voltammetric Surface Dealloying. *J. Am. Chem. Soc.* **2007**, *129*, 12624.

(33) Cui, C.; Gan, L.; Heggen, M.; Rudi, S.; Strasser, P. Compositional segregation in shaped Pt alloy nanoparticles and their structural behaviour during electrocatalysis. *Nat. Mater.* **2013**, *12*, 765.

(34) Strasser, P.; Koh, S.; Anniyev, T.; Greeley, J.; More, K.; Yu, C.; Liu, Z.; Kaya, S.; Nordlund, D.; Ogasawara, H.; Toney, M. F.; Nilsson, A. Lattice-strain control of the activity in dealloyed core—shell fuel cell catalysts. *Nat. Chem.* **2010**, *2*, 454.

(35) Petkov, V.; Maswadeh, Y.; Vargas, J. A.; Shan, S.; Kareem, H.; Wu, Z. P.; Luo, J.; Zhong, C. J.; Shastri, S.; Kenesei, P. Deviations from Vegard's law and evolution of the electrocatalytic activity and stability of Pt-based nanoalloys inside fuel cells by *in operando* X-ray spectroscopy and total scattering. *Nanoscale* **2019**, *11*, 5512.

(36) Liu, M.; Zhao, Z.; Duan, X.; Huang, Y. Nanoscale Structure Design for High-Performance Pt-Based ORR Catalysts. *Adv. Mater.* **2019**, *31*, 1802234.

(37) Luo, M.; Sun, Y.; Zhang, X.; Qin, Y.; Li, M.; Li, Y.; Li, C.; Yang, Y.; Wang, L.; Gao, P.; Lu, G.; Guo, S. Stable High-Index Faceted Pt Skin on Zigzag-Like PtFe Nanowires Enhances Oxygen Reduction Catalysis. *Adv. Mater.* **2018**, *30*, 1705515.

(38) Shui, J.; Chen, C.; Li, J. C. M. Evolution of Nanoporous Pt—Fe Alloy Nanowires by Dealloying and their Catalytic Property for Oxygen Reduction Reaction. *Adv. Funct. Mater.* **2011**, *21*, 3357.

(39) Wang, Y.; Yin, K.; Lv, L.; Kou, T.; Zhang, C.; Zhang, J.; Gao, H.; Zhang, Z. Eutectic-directed self-templating synthesis of PtNi nanoporous nanowires with superior electrocatalytic performance towards the oxygen reduction reaction: experiment and DFT calculation. *J. Mater. Chem. A* **2017**, *5*, 23651.

(40) Petkov, V.; Prasai, B.; Shan, S.; Ren, Y.; Wu, J.; Cronk, H.; Luo, J.; Zhong, C. J. Structural dynamics and activity of nanocatalysts inside fuel cells by *in operando* atomic pair distribution studies. *Nanoscale* **2016**, *8*, 10749.

(41) Wu, Z. P.; Shan, S.; Xie, Z. H.; Kang, N.; Park, K.; Hopkins, E.; Yan, S.; Sharma, A.; Luo, J.; Wang, J.; Petkov, V.; Wang, L.; Zhong, C. J. *ACS Catal.* **2018**, *8*, 11302.

(42) Alia, S. M.; Ngo, C.; Shulda, S.; Ha, M.-A.; Dameron, A. A.; Weker, J. N.; Neyerlin, K. C.; Kocha, S. S.; Pylypenko, S.; Pivovar, B. S. Exceptional Oxygen Reduction Reaction Activity and Durability of Platinum−Nickel Nanowires through Synthesis and Post-Treatment Optimization. *ACS Omega* **2017**, *2*, 1408.

(43) Rudi, S.; Gan, L.; Cui, C.; Gliech, M.; Strasser, P. Electrochemical Dealloying of Bimetallic ORR Nanoparticle Catalysts at Constant Electrode Potentials. *J. Electrochem. Soc.* **2015**, *162*, F403.

(44) Greeley, J.; Nørskov, J. K. Electrochemical dissolution of surface alloys in acids: Thermodynamic trends from first-principles calculations. *Electrochim. Acta* **2007**, *52*, 5829.

(45) Shao, M.; Shoemaker, K.; Peles, A.; Kaneko, K.; Protsailo, L. Pt Monolayer on Porous Pd-Cu Alloys as Oxygen Reduction Electrocatalysts. *J. Am. Chem. Soc.* **2010**, *132*, 9253.

(46) Gan, L.; Heggen, M.; Rudi, S.; Strasser, P. Core−Shell Compositional Fine Structures of Dealloyed Pt_xNi_{1-x} Nanoparticles and Their Impact on Oxygen Reduction Catalysis. *Nano Lett.* **2012**, *12*, 5423.

(47) Francis, M. F.; Curtin, W. A. Mechanical work makes important contributions to surface chemistry at steps. *Nat. Commun.* **2015**, *6*, 6261.

(48) Jia, Q.; Caldwell, K.; Strickland, K.; Ziegelbauer, J. M.; Liu, Z.; Yu, Z.; Ramaker, D. E.; Mukerjee, S. Improved Oxygen Reduction Activity and Durability of Dealloyed $PtCo_x$ Catalysts for Proton Exchange Membrane Fuel Cells: Strain, Ligand, and Particle Size Effects. *ACS Catal.* **2015**, *5*, 176.

(49) Popov, B. N. *Annual Merit Review DOE Hydrogen and Fuel Cells and Vehicle Technologies Programs*. http://www.hydrogen.energy.gov/pdfs/review14/fc088_popov_2014_o.pdf, 2014; Accessed September 2015.

(50) Steinbach, A *Annual Merit Review DOE Hydrogen and Fuel Cells and Vehicle Technologies Programs*. http://www.hydrogen.energy.gov/pdfs/review14/fc104_steinbach_2014_o.pdf, 2014; Accessed September 2015.

(51) Kuhl, S.; Strasser, P. Oxygen Electrocatalysis on Dealloyed Pt Nanocatalysts. *Top. Catal.* **2016**, *59*, 1628.

(52) Ratso, S.; Ranjbar Sahraie, N.; Sougrati, M. T.; Käärik, M.; Kook, M.; Saar, R.; Paiste, P.; Jia, Q.; Leis, J.; Mukerjee, S.; Jaouen, F.; Tammeveski, K. *J. Mater. Chem. A* **2018**, *6*, 14663.

(53) Fang, B.; Luo, J.; Njoki, P. N.; Loukrakpam, R.; Wanjala, B.; Hong, J.; Yin, J.; Hu, X.; Last, J.; Zhong, C. J. *Electrochim. Acta* **2010**, *55*, 8230.

(54) Becknell, N.; Son, Y.; Kim, D.; Li, D.; Yu, Y.; Niu, Z.; Lei, T.; Sneed, B. T.; More, K. L.; Markovic, N. M.; Stamenkovic, V. R.; Yang, P. *J. Am. Chem. Soc.* **2017**, *139*, 11678.